

Beyond ^{18}F -FDG: Characterization of PET/CT and PET/MR Scanners for a Comprehensive Set of Positron Emitters of Growing Application— ^{18}F , ^{11}C , ^{89}Zr , ^{124}I , ^{68}Ga , and ^{90}Y

A. Therese Soderlund¹, Jasper Chaal¹, Gabriel Tjio¹, John J. Totman¹, Maurizio Conti², and David W. Townsend^{1,3}

¹A*STAR-NUS Clinical Imaging Research Center, Singapore; ²Siemens Healthcare Molecular Imaging, Knoxville, Tennessee; and

³Department of Diagnostic Radiology, National University Hospital, Singapore

This study aimed to investigate image quality for a comprehensive set of isotopes (^{18}F , ^{11}C , ^{89}Zr , ^{124}I , ^{68}Ga , and ^{90}Y) on 2 clinical scanners: a PET/CT scanner and a PET/MR scanner. **Methods:** Image quality and spatial resolution were tested according to NU 2-2007 of the National Electrical Manufacturers Association. An image-quality phantom was used to measure contrast recovery, residual bias in a cold area, and background variability. Reconstruction methods available on the 2 scanners were compared, including point-spread-function correction for both scanners and time of flight for the PET/CT scanner. Spatial resolution was measured using point sources and filtered backprojection reconstruction. **Results:** With the exception of ^{90}Y , small differences were seen in the hot-sphere contrast recovery of the different isotopes. Cold-sphere contrast recovery was similar across isotopes for all reconstructions, with an improvement seen with time of flight on the PET/CT scanner. The lower-statistic ^{90}Y scans yielded substantially lower contrast recovery than the other isotopes. When isotopes were compared, there was no difference in measured spatial resolution except for PET/MR axial spatial resolution, which was significantly higher for ^{124}I and ^{68}Ga . **Conclusion:** Overall, both scanners produced good images with ^{18}F , ^{11}C , ^{89}Zr , ^{124}I , ^{68}Ga , and ^{90}Y .

Key Words: positron emission tomography; image quality; contrast recovery; spatial resolution; radionuclide therapy

J Nucl Med 2015; 56:1285–1291

DOI: 10.2967/jnumed.115.156711

T

he first isotopes used in PET were those of elements common in the human body, such as ^{15}O , ^{13}N , and ^{11}C . They found applications in both research and clinical PET: ^{15}O measured brain blood flow (1); ^{13}N assessed myocardial perfusion (2); and ^{11}C was successful in several applications, such as brain tumor imaging (3), prostate cancer staging (4), and cardiology (5). The short half-lives of these isotopes require an on-site cyclotron, a limiting factor for their widespread use.

PET grew rapidly from the late 1990s. Approval for reimbursement by the Centers for Medicare and Medicaid Services, the longer

half-life of ^{18}F , and the simple uptake mechanism of ^{18}F -FDG were key factors for general use in oncology and other fields. More recently, ^{82}Rb found widespread applications in myocardial perfusion studies (6), and ^{68}Ga has been extensively used for somatostatin receptor imaging (7). Both are generator-produced and can therefore be used by PET centers without access to a cyclotron.

The continuous evolution of PET is now bringing new applications for old positron-emitting isotopes. In oncology, molecular imaging is evolving from simply tracking the hypermetabolism of cancer cells into imaging target molecules specific to a unique mechanism, or monitoring and guiding medical therapy, as in immunotherapy and radioimmunotherapy (8,9). Monoclonal antibodies are growing dramatically as therapeutic target-specific agents (10); ^{124}I , ^{89}Zr , ^{86}Y , ^{76}Br , and ^{64}Cu have shown an excellent ability to label monoclonal antibodies, with half-lives matched to the rate of antibody accumulation in tumors or target organs. Another area of development is targeted radionuclide therapy—for example, companion diagnostics with ^{124}I imaging providing pretreatment assessment for ^{131}I -targeted radiotherapy (11) and localized microsphere treatment of liver cancer being performed with ^{90}Y (12).

Although ^{18}F is characterized by pure β^+ decay and a short-range positron, some non- ^{18}F tracers are challenging for PET scanners. ^{68}Ga , ^{15}O , ^{82}Rb , ^{76}Br , ^{86}Y , and ^{124}I emit higher-energy positrons (longer range), which is a potential limit for the achievable PET spatial resolution, and for ^{64}Cu , ^{89}Zr , ^{76}Br , ^{86}Y , and ^{124}I , β^+ decay is not the preferential decay mechanism. ^{90}Y has a positron-emitting branching ratio of only a few parts per million and a high flux of Bremsstrahlung photons, creating high singles rates and high randoms fractions (13,14). For ^{82}Rb , ^{76}Br , ^{86}Y , ^{124}I , and ^{89}Zr , γ rays are emitted in coincidence with the β^+ decay. If such γ rays are detected and fall into the PET energy and time windows, they cannot be distinguished from coincidence photons. In this case there is no colinearity, resulting in diffuse background and quantification errors in the image unless proper corrections are implemented (15,16).

The performance of clinical PET scanners using ^{18}F is routinely presented (17,18). Much less is available in the literature on non- ^{18}F imaging performance, and in general the image quality is assessed for a specific isotope or application: ^{124}I (19–21), ^{89}Zr (22,23), ^{64}Cu (23), ^{90}Y (12–14), ^{76}Br (21), or ^{86}Y (19,20). The performance of small-animal and high-resolution PET scanners with ^{18}F , ^{68}Ga , ^{124}I , and ^{89}Zr have, however, been investigated (24,25).

The aim of this study was to investigate image quality and spatial resolution for a comprehensive set of non- ^{18}F isotopes on 2 clinical scanners: a PET/CT scanner and a PET/MR scanner. We also investigated the difference in performance seen for different

Received Mar. 3, 2015; revision accepted Jun. 23, 2015.

For correspondence or reprints contact: Therese Soderlund, A*STAR-NUS Clinical Imaging Research Centre, Centre for Translational Medicine, 14 Medical Dr., B1-01, Singapore 117599.

E-mail: anna_therese@circ.a-star.edu.sg

Published online Jul. 1, 2015.

COPYRIGHT © 2015 by the Society of Nuclear Medicine and Molecular Imaging, Inc.

reconstruction strategies available on each imaging platform. All studies were performed using the same consistent methodology and experimental apparatus, allowing for a unique and fair comparison between isotopes.

MATERIALS AND METHODS

PET Scanners

Measurements were performed on a Biograph mCT PET/CT scanner and a Biograph mMR PET/MR scanner (Siemens). Specifications for the PET scanners are shown as supplemental material (supplemental materials are available at <http://jnm.snmjournals.org>). Both scanners have lutetium oxyorthosilicate crystals, coupled to photomultiplier tubes on the mCT and avalanche photodiodes on the mMR. Although time-of-flight (TOF) reconstruction is available on the mCT, the slower timing characteristics of avalanche photodiodes preclude this option on the mMR. Both scanners allow for analytic and iterative reconstruction. Two-dimensional filtered backprojection (FBP) was used, after Fourier rebidding into direct planes. The iterative method is based on ordinary Poisson ordered-subsets expectation maximization (OP-OSEM), with point spread function (PSF) modeling on both scanners. In this work the manufacturer's default iterations and subsets were used (Table 1).

On the mCT, attenuation correction is derived from CT, whereas on the mMR, a Dixon MR sequence is used to generate a segmented attenuation map. Because the Dixon attenuation map for an image-quality phantom filled with water is prone to artifacts (26), the CT-based attenuation map was registered to the mMR PET image position and used for mMR attenuation correction. This is the standard procedure used for NEMA performance measurements on the mMR.

Isotopes

The physical properties of the isotopes selected for this study are shown in Table 2. ^{18}F was chosen because it is the standard isotope used in NEMA NU 2-2007 (27) and as such can be used as a reference against which the performance of other isotopes can be evaluated. ^{11}C was included because of its widespread use in a variety of research applications, whereas ^{124}I , ^{89}Zr , ^{68}Ga , and ^{90}Y were chosen for their increased use in targeted radiotherapy, immunotherapy, and highly specific tracer imaging.

^{18}F -fluoride, ^{68}Ga -chloride, and ^{11}C -acetate were acquired from Singapore Radiopharmaceuticals Pte. Ltd., whereas ^{124}I -NaOH, ^{89}Zr -oxalic acid, and ^{90}Y -chloride were obtained from Perkin Elmer. To prevent ^{124}I , ^{89}Zr , and ^{90}Y from sticking to the plastic of the image-quality phantom, the solutions had to be prepared further. For ^{124}I -NaOH, the phantom was filled with a 20 mM NaOH solution, whereas a 1 M diethylenetriamine pentaacetic acid solution was used for ^{90}Y . ^{89}Zr -oxalic acid was neutralized using 2 M Na_2CO_3 , followed by addition of a calibration mixture containing 0.2 M HEPES ((4-(2-hydroxyethyl)-

1-piperazineethanesulfonic acid) and a 1 mg/mL concentration of bovine serum albumin in phosphate-buffered saline.

Performance Measurements

Performance was measured according to the image-quality and spatial resolution tests outlined in NEMA NU 2-2007 (27), with some adjustments as described below.

Image Quality. Image quality was assessed using a NEMA IEC body phantom (Data Spectrum Corp.). The torso-shaped phantom consists of 6 fillable spheres (internal diameters: 10, 13, 17, 22, 28, and 37 mm) aligned in a transaxial plane of the phantom. To simulate lung attenuation, a low-atomic-number cylindric insert (outside diameter, 50 ± 2 mm) is centered inside the phantom. For all isotopes, the 2 largest spheres were filled with water (cold lesions), whereas the remaining spheres were filled with radioactivity to mimic hot lesions. The background compartment of the phantom and the hot lesions were filled to get a lesion-to-background ratio of 4:1. This study did not use the NEMA NU-2 2007 standard specification that a scatter phantom containing an ^{18}F line source should be placed adjacent to the body phantom.

To obtain images of comparable noise level, a single-bed acquisition of 200 million net true counts was performed for all isotopes except ^{90}Y . Because the mMR has higher sensitivity, the mCT scans were performed first. Because of the different branching ratios, decay times, and starting activities, each experiment required a different acquisition time (the starting time of the mCT PET scan was set as the reference time for all assays): 58 MBq of ^{18}F , 10 min on the mCT and 9 min on the mMR; 51 MBq of ^{11}C , 14 min on the mCT and 24 min on the mMR; 41 MBq of ^{89}Zr , 59 min on the mCT and 44 min on the mMR; 32 MBq of ^{124}I , 66 min on the mCT and 49 min on the mMR; 40 MBq of ^{68}Ga , 17 min on the mCT and 21 min on the mMR. Because of the low positron emission probability of ^{90}Y , a higher activity concentration was used and it was still not possible to acquire 200 million net true counts in a reasonable scanning time. For ^{90}Y , the assay activity was 1,074 MBq and a 12-h scanning time was used to acquire 7.9 and 11.5 million net true counts (at 88% and 82% random fraction) on the mCT and mMR, respectively.

We performed iterative reconstruction according to Table 1 at full resolution (400×400 transaxial pixels for mCT and 344×344 for mMR; image pixel size, 2 mm). A gaussian postreconstruction filter of 2 mm in full width at half maximum (FWHM) was applied, and the axial slices were 2 mm thick. The data were corrected for scatter, randoms, attenuation, dead time, decay, and normalization. Prompt γ correction was applied for ^{124}I . The reconstructed images were analyzed using an in-house script written in MATLAB (release 2012b; The MathWorks Inc.). Cold and hot contrast recoveries, background variability, and residual bias in the lung insert were calculated according to NEMA NU 2-2007.

TABLE 1
Available Reconstruction Methods

Method	mCT*	mMR*
FBP	Backprojection	Filtered backprojection
FBP+TOF	Backprojection+TOF	—
3D OP-OSEM	Iterative (3 iterations, 24 subsets)	3D iterative (3 iterations, 21 subsets)
3D OP-OSEM+TOF	Iterative+TOF (2 iterations, 21 subsets)	—
3D OP-OSEM+PSF	TrueX (3 iterations, 24 subsets)	HD PET (3 iterations, 21 subsets)
3D OP-OSEM+PSF+TOF	TrueX+TOF (2 iterations, 21 subsets)	—

*Reconstruction label in user interface.

TABLE 2
Properties of Positron-Emitting Isotopes Used in This Work (37–39)

Property	¹⁸ F	¹¹ C	⁸⁹ Zr	¹²⁴ I	⁶⁸ Ga	⁹⁰ Y
Half-life	109.8 min	20.4 min	78.4 h	100.2 h	67.6 min	64.1 h
β^+ , decay fraction (%)	97	100	23	23	88	0.0032*
β^+ , mean energy (MeV)	0.250	0.386	0.396	0.832	0.836	<0.769†
β^+ , mean range, water (mm)	0.64	1.22	1.27	3.46	3.49	—
Prompt γ emission‡	No	No	No	Yes (0.603 MeV)	No	No§

* β branching ratio for production of $e^+ e^-$ pairs.

† β maximum energy available for $e^+ e^-$ pairs.

‡Prompt γ emission within PET energy window.

§High singles photon counting rate from Bremsstrahlung (not in coincidence).

Spatial Resolution. Spatial resolution was measured using glass capillary tubes (inner diameter, 1.0 mm; wall thickness, 0.3 mm; length, 75 mm). Absorbing resin limited the axial extent of the radioactivity to about 1.5 mm. The radioactivity at the start of image acquisition for the first scan of each isotope was 4.8 MBq for ¹⁸F, 5.3 MBq for ¹¹C, 3.8 MBq for ⁸⁹Zr, 2.9 MBq for ¹²⁴I, and 5.0 MBq for ⁶⁸Ga. Two separate sources of 25.7 MBq for the mCT and 1.6 MBq for the mMR were used for ⁹⁰Y. Using in-house manufactured jigs, the capillary was positioned parallel to the scanner axis with the source in air. Data were acquired with the scanner beds retracted from the field of view and with the point source located at 2 axial positions: at the center of the field of view and 59 mm and 65 mm off-center for the mCT and mMR, respectively (one-quarter field of view off-center). At each axial position, measurements were performed at transaxial positions (1,0), (10,0), and (0,10) cm. Two million net true counts were acquired at each position for all isotopes except ⁹⁰Y. Because of the low probability of positron emission for ⁹⁰Y, 0.15 and 0.065 million net true counts were acquired on the mCT and mMR, respectively (98% random fraction for both scanners). Three acquisitions were performed at each position. The SD was calculated and used as an estimate of the measurement error. Because of the short half-life of ¹¹C and the long imaging times of ⁹⁰Y, only one measurement per position was possible and error measurements were not obtained.

Data were reconstructed using FBP at full resolution (400 × 400 transaxial pixels for mCT and 344 × 344 for mMR; pixel size, 2 mm) and corrected for randoms, dead time, decay, and normalization. MATLAB was used to measure the spatial resolution in terms of FWHM and full width at tenth maximum (FWTM) according to NEMA NU-2 2007. FWHM-to-FWTM ratios were also calculated.

RESULTS

Image Quality

For a visual comparison, images of the center slice for all isotopes and both scanners are shown in Figure 1. The measured hot and cold sphere contrast recoveries are tabulated as supplemental material and shown in Figures 2 and 3 for all isotopes and reconstruction methods. Because of the fewer counts acquired for ⁹⁰Y and the high proportion of Bremsstrahlung, the quality of the ⁹⁰Y reconstructed data was poorer than that for the other isotopes. Contrast recovery was calculated only for spheres that were actually visible in the ⁹⁰Y datasets. Figures 4 and 5 show the residual bias in the lung insert and the background variability for the 37-mm sphere for all isotopes.

With the exception of ⁹⁰Y and to a lesser extent ¹²⁴I, small differences were seen in the contrast recovery performance of

the different isotopes. However, for the smaller hot spheres a general trend of contrast recovery being dependent on the positron range of the isotope was observed, with ¹⁸F showing the best performance and ⁶⁸Ga and ¹²⁴I showing the overall poorest performance. The cold sphere contrast recovery was similar across isotopes and different reconstruction methods. As expected, ⁹⁰Y had substantially lower contrast recovery results than the other isotopes, and the 10-mm sphere was not visible for all reconstructions. In general, cold sphere contrast recovery was lower on the mMR than on the mCT. When TOF was added to reconstruction on the mCT, contrast recovery performance improved. This was expected because TOF leads to faster reconstruction convergence.

No relevant difference between isotopes was observed for the lung insert residual bias (again, with the exception of ⁹⁰Y), but a variation was found between reconstruction methods. For the mCT, TOF lowered the residual bias, whereas PSF did not bring about any change. PSF also did not change the residual bias on the

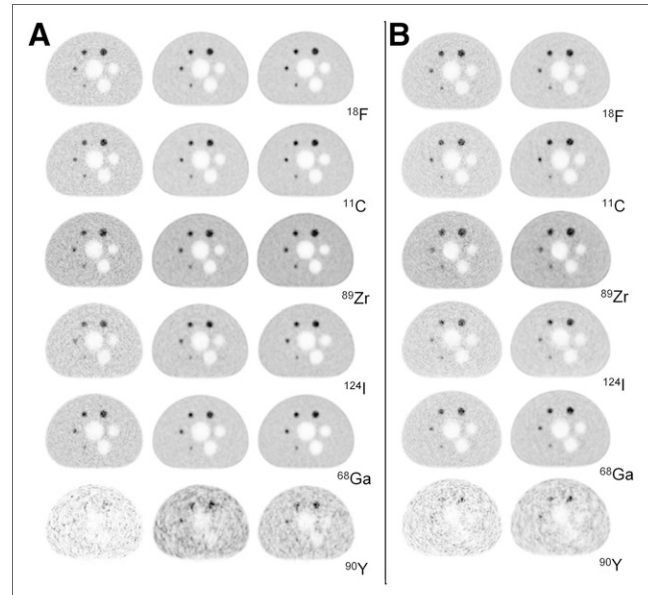


FIGURE 1. PET images reconstructed for all isotopes. (A) Images obtained on mCT using 3D OP-OSEM (left), 3D OP-OSEM+PSF (center), and 3D OP-OSEM+PSF+TOF (right). (B) Images obtained on mMR using 3D OP-OSEM (left) and 3D OP-OSEM+PSF (right). All images have 2-mm pixel size and 2-mm postreconstruction gaussian filter applied.

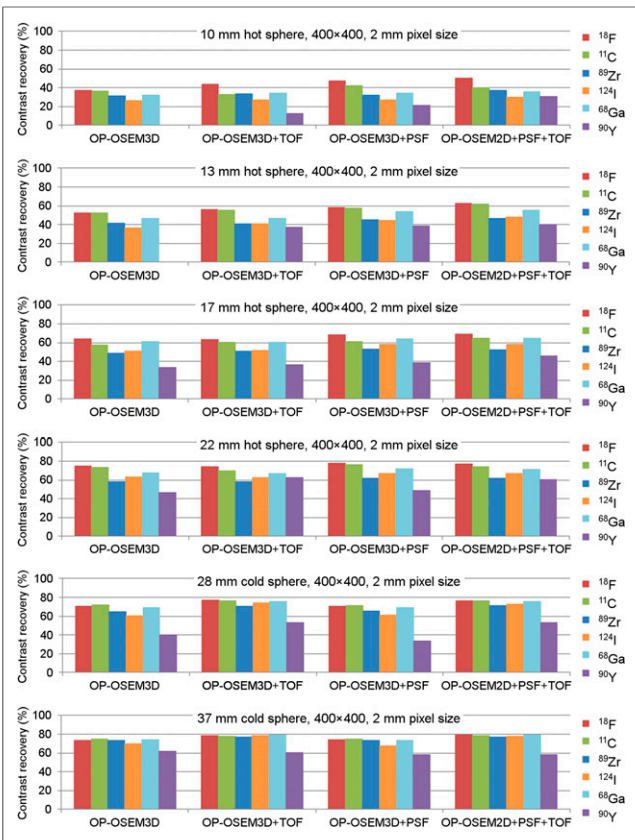


FIGURE 2. mCT contrast recovery for all isotopes. ⁹⁰Y data were omitted from plot when sphere was not visible in image.

mMR. The mCT and mMR had equal performance regarding residual bias. ⁹⁰Y and ¹²⁴I had a poorer background variability performance than the other isotopes, ⁹⁰Y to a much larger extent than ¹²⁴I. Possible inaccuracies in the prompt γ correction could be the reason for the slightly worse performance of ¹²⁴I. For ⁹⁰Y this can be attributed mainly to the much lower number of counts acquired and the correspondingly higher noise level. To correct for the lower count statistics, count normalization to 200 million net true counts was performed for the ⁹⁰Y data (measured background variability times the square root of the net true counts in the scan divided by 200 million). The count normalization brought the background variability closer to that of the remaining isotopes, decreasing it by a factor of approximately 5 (Figs. 4 and 5). The choice of reconstruction did not greatly change the background variability.

Spatial Resolution

The axial and transverse spatial resolution results are shown in Figures 6 and 7 and are tabulated as supplemental material. When FWHM was compared across isotopes, the positron range had little if any effect on the measured spatial resolution. The exception was that the axial spatial resolution at 1 and 10 cm measured on the mMR was significantly higher for ¹²⁴I and ⁶⁸Ga. For ⁹⁰Y, the spatial resolution results were similar to those for the other isotopes even though substantially fewer counts were acquired.

The FWHM-to-FWTM ratios for the mCT and mMR (Fig. 7) can be compared with a ratio of 0.55, which is expected for a gaussian distribution (24). Measurements performed on the mCT gave fairly good approximations of the expected ratio for

all isotopes. For the mMR, lower ratios were, however, measured in the transverse tangential direction for all isotopes and in the axial direction for the longer positron-range isotopes ¹²⁴I and ⁶⁸Ga. This finding indicates extended tails in the distribution, as also observed for the FWTM results (supplemental material).

DISCUSSION

In this study we investigated image quality parameters for 2 clinical scanners—the Biograph mCT PET/CT scanner and the Biograph mMR PET/MR scanner—for a range of clinically interesting isotopes. As the number of isotopes used for PET imaging increases, it becomes increasingly important to validate PET scanner performance for isotopes other than ¹⁸F. The NEMA NU-2 2007 tests provide a simplified setting in which the performance

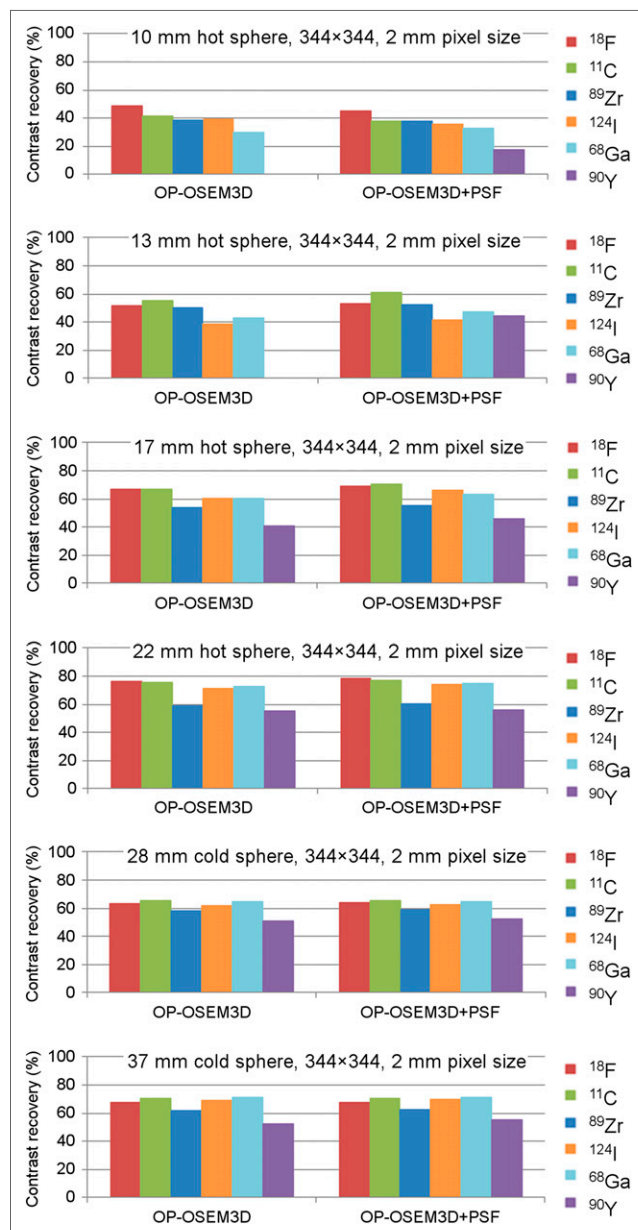


FIGURE 3. mMR contrast recovery for all isotopes. ⁹⁰Y data were omitted from plot when sphere was not visible in image.

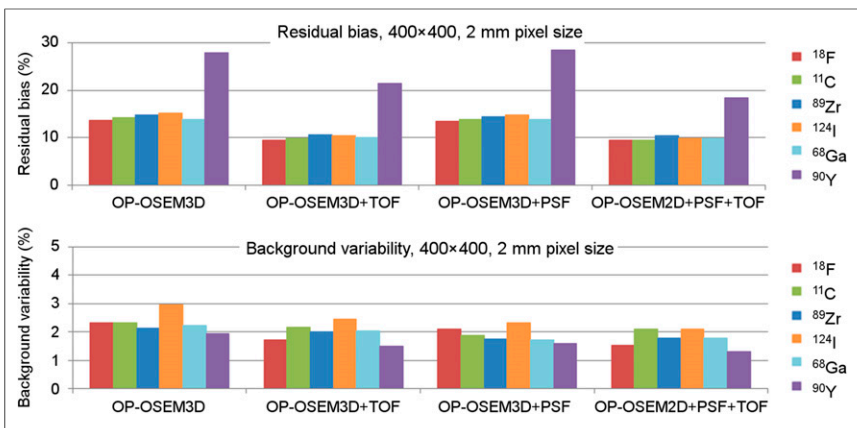


FIGURE 4. mCT residual bias in lung insert and background variability. For background variability, ^{90}Y data have been normalized to 200-million-true-count scan.

of scanners for a range of isotopes can be evaluated and compared, even though the tests do not directly assess performance under realistic clinical conditions. Performance measurements for the mCT and mMR using ^{18}F have previously been performed (17,18). For both studies, image-quality phantom scanning times and activities were approximately the same as used in this work, giving similar count statistics. The contrast recovery, background variability, and residual bias measured in this study were compatible with those reported. The minor differences were most likely due to reconstruction parameters: fewer iterations and filters reduce contrast recovery and background variability, for example. From the point of view of spatial resolution, again, the ^{18}F measurements were in full agreement with the literature.

This study showed small differences in image quality and spatial resolution performance between isotopes. With the exception of ^{90}Y , the isotopes had performance characteristics similar to those of the gold standard, ^{18}F . Because of the low positron-emitting branching ratio (and as a result the poorer count statistics achieved), as well as the high flux of Bremsstrahlung, the measured contrast recovery, background variability, and residual bias were lower for ^{90}Y than for the other isotopes. This was, however,

not seen for the spatial resolution data, for which ^{90}Y measurements were as expected given the positron range of this isotope (maximum positron energy similar to that of ^{11}C).

Although a trend of decreased contrast recovery with increased positron range was observed for small spheres, the overall difference between isotopes was small. This observation was most likely due to the spatial resolution limitations of current clinical PET scanners, on the order of 4 mm, and can be contrasted to similar studies using high-resolution animal scanners in which an effect of positron range on contrast recovery has been shown (24,25,28). As expected, large-sphere contrast recovery and residual bias in the lung insert show no effect of positron range. Both are, however, affected by

the reconstruction method, with TOF shown to improve recovery of cold areas.

^{124}I performed slightly less well than the other isotopes (apart from ^{90}Y) with regard to background variability (Figs. 4 and 5). This finding can potentially be explained by the prompt γ emission associated with this isotope, not perfectly corrected by the model for prompt γ used. On the other hand, the measured background variability for ^{124}I was still limited to about 3%–4%, compared with 2%–3% for the other isotopes, and no image artifacts were visually detected. Other studies also demonstrate good quantification of ^{124}I distribution when proper prompt γ correction is applied (29).

^{90}Y is a challenging isotope, as we confirmed by the lower contrast recovery measured (Figs. 2 and 3) and by high residual bias in the lung insert and background variability (Figs. 4 and 5). These challenging characteristics have also been found by other groups (13). A major reason for this decreased performance is obviously the lower statistics in the ^{90}Y scan, which reduce the signal-to-noise ratio and affect imaging from different points of view. On the other hand, the typical clinical conditions for ^{90}Y require imaging at extremely low statistics, typically less than 1×10^6 counts per scan (13,14), and it is therefore fair to test the systems at this count level. Lower counts affect the detectability of small lesions, as the smallest spheres in our data were hardly visible; background variability is higher because of the increased noise level; and residual bias in cold areas is increased because of poor convergence and algorithm bias at extremely low counts (30). Lower statistics alone are not the only reason for the poorer performance of ^{90}Y . The high randoms fraction of ^{90}Y scans—due to Bremsstrahlung photons and the natural background radioactivity in lutetium oxyorthosilicate scintillators—has a multiply negative effect on image quality: the scatter estimate is less reliable, the accuracy of randoms correction has a stronger effect on the image, and the limitations of the reconstruction algorithms affect the resulting image (31). Inaccurate data corrections for scatter and randoms are responsible for additional noise, and a major limitation comes from the nonnegativity constraint of the MLEM-based reconstruction algorithm: the stochastic nature of the random-coincidence events can produce more random than prompt counts in many sinogram elements, and the truncation of the negative image values to zero is responsible for a positive and noisy bias in the background. Such positive biases strongly affect and decrease contrast recovery

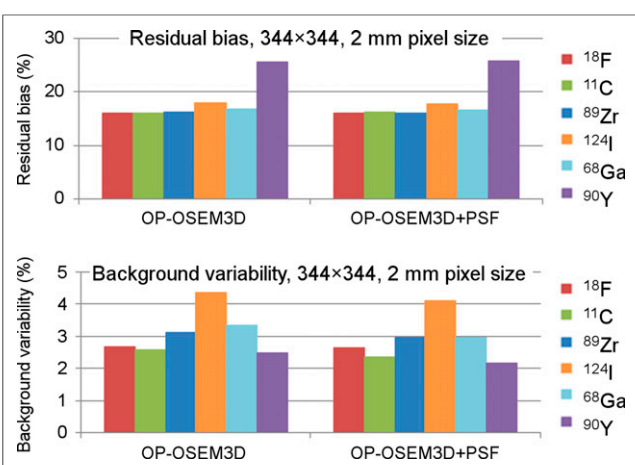


FIGURE 5. mMR residual bias in lung insert (top) and background variability (bottom). For background variability, ^{90}Y data have been normalized to 200-million-true-count scan.

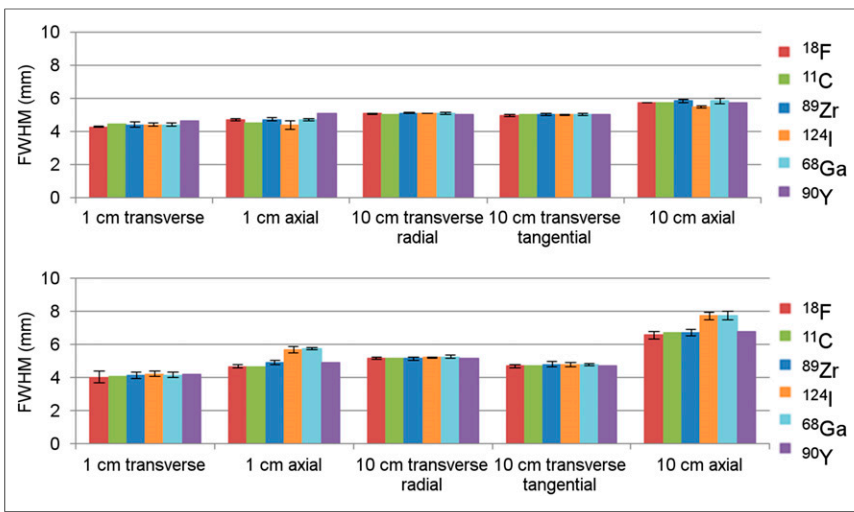


FIGURE 6. mCT (top) and mMR (bottom) FWHM measurements (2-mm pixel size) obtained with FBP and no postreconstruction filter. Error bars are 2 times SD of repeated measurements.

(31–33). On the other hand, it has been observed that TOF reconstruction reduces this phenomenon (31,32). In this work, TOF reconstruction was shown to reduce the cold-area bias and background variability for ⁹⁰Y (Figs. 4 and 5).

A limitation of this study was the lack of error estimates for the contrast recovery data. However, error was measured by calculating the SE for the ¹⁸F data by scanning the image-quality phantom using an extended list-mode scan, followed by creation of 10 random realizations of 200 million net true counts. Overall, the contrast recovery SE over the 10 measurements was small, with the largest errors measured for the 10-mm hot sphere. For example, the SEs of the contrast recovery measurements for the 10-mm sphere, for the mCT 3-dimensional (3D) OP-OSEM and 3D OP-OSEM+PSF+TOF reconstructions, were 1.6% and 1.0%, respectively. Because the same count statistics were used for all isotopes, it is expected that the errors would also be low for the non-¹⁸F isotopes. The exception is ⁹⁰Y, for which the error is likely to be larger. In general, error measurements are typically not used for NEMA contrast recovery measurements, and

the data presented in this paper are therefore comparable to previously reported contrast recovery studies.

Regarding spatial resolution, minor differences were observed between isotopes in the transverse direction. Studies using high-resolution animal scanners (24,25) and simulations (34) have shown that a resolution dependence on positron range does exist. The resolution capabilities of modern clinical whole-body PET systems are, however, too low to allow this difference to be measured. Indeed, the measured spatial resolutions of both systems in this study were greater than the mean positron ranges of the isotopes used. High-resolution animal systems also show decreased FWHM-to-FWTM ratios for isotopes with a longer positron range, such as ⁶⁸Ga and ¹²⁴I (24,25). This feature, however, was not seen for the mCT and mMR, again most

likely because of the poorer spatial resolution of these clinical systems.

The axial spatial resolution of the mMR was higher than the transverse spatial resolution for all isotopes, and remarkably so for the long-positron-range isotopes ⁶⁸Ga and ¹²⁴I (Fig. 6). In addition, decreased FWHM-to-FWTM ratios were observed, indicating increased tails as measured by the FWTM (Fig. 7). It is known that a magnetic field has the effect of constraining the positron range in the transverse direction and spreading it in the axial direction; “collimated” positron beams in a PET/MR scanner have been observed and studied (35). An explanation for this behavior was offered by Kraus et al. (36) whereby events that would otherwise lie on different planes drift into the axial direction, with the effect of a broadening of the axial distribution profile and an alteration of the distribution shape, with increased tails. This helicoid drift was also shown to give a distribution spread in the transverse tangential direction and was observed for all isotopes in the presence of the magnetic field, with increased FWTMs and decreased FWHM-to-FWTM ratios (Fig. 7). This was also shown by Delso et al. (18), who measured a similar FWHM-to-FWTM ratio when using ¹⁸F.

CONCLUSION

Overall, ¹¹C, ⁸⁹Zr, ¹²⁴I, ⁶⁸Ga, and ⁹⁰Y produce good images on both the mCT and the mMR, having imaging performance parameters similar to those of the reference isotope, ¹⁸F. Differences in positron range do not have a strong effect at the typical spatial resolution of the clinical PET scanners. In the mMR, however, the magnetic field slightly broadened the axial spatial resolution for high-energy positron emitters (¹²⁴I and ⁶⁸Ga).

DISCLOSURE

The costs of publication of this article were defrayed in part by the payment of

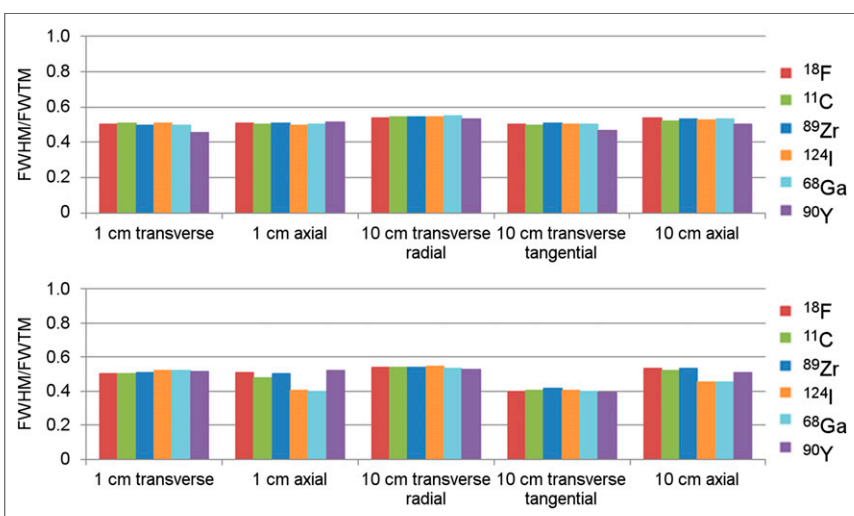


FIGURE 7. mCT (top) and mMR (bottom) FWHM-to-FWTM ratios (2-mm pixel size) obtained with FBP and no postreconstruction filter.

page charges. Therefore, and solely to indicate this fact, this article is hereby marked “advertisement” in accordance with 18 USC section 1734. Maurizio Conti is an employee of Siemens Healthcare Molecular Imaging in Knoxville, Tennessee. David Townsend receives royalties from Siemens Healthcare Molecular Imaging for the invention of the PET/CT scanner. No other potential conflict of interest relevant to this article was reported.

ACKNOWLEDGMENT

We thank Prof. Dale Bailey at the Royal North Shore Hospital, Australia, for providing the image-quality phantom used in this study.

REFERENCES

- Mintun MA, Raichle ME, Martin WR, Herscovitch P. Brain oxygen utilization measured with O-15 radiotracers and positron emission tomography. *J Nucl Med*. 1984;25:177–187.
- Schelbert HR, Phelps ME, Huang SC, et al. N-13 ammonia as an indicator of myocardial blood flow. *Circulation*. 1981;63:1259–1272.
- Becherer A, Karanikas G, Szabó M, et al. Brain tumour imaging with PET: a comparison between [¹⁸F]fluorodopa and [¹¹C]methionine. *Eur J Nucl Med Mol Imaging*. 2003;30:1561–1567.
- Hara T, Kosaka N, Kishi H. PET imaging of prostate cancer using carbon-11-choline. *J Nucl Med*. 1998;39:990–995.
- Pike VW, Eakins MN, Allan RM, Selwyn AP. Preparation of [1-¹¹C]acetate: an agent for the study of myocardial metabolism by positron emission tomography. *Int J Appl Radiat Isot*. 1982;33:505–512.
- Di Carli MF, Dorbala S, Meserve J, El Fakhri G, Sitek A, Moore SC. Clinical myocardial perfusion PET/CT. *J Nucl Med*. 2007;48:783–793.
- Al-Nahhas A, Win Z, Szyszko T, et al. Gallium-68 PET: a new frontier in receptor cancer imaging. *Anticancer Res*. 2007;27:4087–4094.
- Verel I, Visser GW, van Dongen GA. The promise of immuno-PET in radioimmunotherapy. *J Nucl Med*. 2005;46(suppl):164S–171S.
- Zalutsky MR. Potential of immuno-positron emission tomography for tumor imaging and immunotherapy planning. *Clin Cancer Res*. 2006;12:1958–1960.
- Reichert JM. Monoclonal antibodies as innovative therapeutics. *Curr Pharm Biotechnol*. 2008;9:423–430.
- Fu D-X, Tanheho YC, Chen J, et al. Virus-associated tumor imaging by induction of viral gene expression. *Clin Cancer Res*. 2007;13:1453–1458.
- Lhommel R, van Elmpt L, Goffette P, et al. Feasibility of ⁹⁰Y TOF PET-based dosimetry in liver metastasis therapy using SIR-Spheres. *Eur J Nucl Med Mol Imaging*. 2010;37:1654–1662.
- Willows K, Forwood N, Jakoby BW, Smith AM, Bailey DL. Quantitative ⁹⁰Y image reconstruction in PET. *Med Phys*. 2012;39:7153–7159.
- Carlier T, Eugène T, Bodet-Milin C, et al. Assessment of acquisition protocols for routine imaging of Y-90 using PET/CT. *EJNMMI Res*. 2013;3:11.
- Surti S, Scheuermann R, Karp JS. Correction technique for cascade gammas in I-124 imaging on a fully-3D, time-of-flight PET scanner. *IEEE Trans Nucl Sci*. 2009;56:653–660.
- Watson C, Hayden C, Casey M, Hamill J, Bendriem B. Prompt gamma correction for improved quantification in ⁸²Rb PET [abstract]. *J Nucl Med*. 2008;49(suppl):64P.
- Jakoby BW, Bercier Y, Conti M, Casey ME, Bendriem B, Townsend DW. Physical and clinical performance of the mCT time-of-flight PET/CT scanner. *Phys Med Biol*. 2011;56:2375–2389.
- Delso G, Furst S, Jakoby B, et al. Performance measurements of the Siemens mMR integrated whole-body PET/MR scanner. *J Nucl Med*. 2011;52:1914–1922.
- Lubberink M, Herzog H. Quantitative imaging of ¹²⁴I and ⁸⁶Y with PET. *Eur J Nucl Med Mol Imaging*. 2011;38(suppl):S10–S18.
- Herzog H, Tellmann L, Scholten B, Coenen HH, Qaim SM. PET imaging problems with the non-standard positron emitters yttrium-86 and iodine-124. *Q J Nucl Med Mol Imaging*. 2008;52:159–165.
- Sandström M, Tolmachev V, Kairemo K, Lundqvist H, Lubberink M. Performance of coincidence imaging with long-lived positron emitters as an alternative to dedicated PET and SPECT. *Phys Med Biol*. 2004;49:5419–5432.
- Makris NE, Boellaard R, Visser EP, et al. Multicenter harmonization of ⁸⁹Zr PET/CT performance. *J Nucl Med*. 2014;55:264–267.
- Laforest R, Liu X. Image quality with non-standard nuclides in PET. *Q J Nucl Med Mol Imaging*. 2008;52:151–158.
- Disselhorst JA, Brom M, Laverman P, et al. Image-quality assessment for several positron emitters using the NEMA NU 4-2008 standards in the Siemens Inveon small-animal PET scanner. *J Nucl Med*. 2010;51:610–617.
- De Jong HWAM, Perk L, Visser GWM, Boellaard R, van Dongen GAMS, Lammertsma AA. High resolution PET imaging characteristics of ⁶⁸Ga, ¹²⁴I and ⁸⁹Zr compared to ¹⁸F. *IEEE Nucl Sci Conf Rec*. 2005;3:1624–1627.
- Ziegler S, Braun H, Ritt P, Hocke C, Kuwert T, Quick HH. Systematic evaluation of phantom fluids for simultaneous PET/MR hybrid imaging. *J Nucl Med*. 2013;54:1464–1471.
- NEMA standards publication NU 2-2007: performance measurements of positron emission tomographs. Arlington, VA: National Electrical Manufacturers Association. 2007.
- Canadas M, Sanz ER, Vives MO, et al. Performance evaluation for ⁶⁸Ga and ¹⁸F of the ARGUS small-animal PET scanner based on the NEMA NU-4 standard. *IEEE Nucl Sci Conf Rec*. 2010;34543457.
- Preylowski V, Schlögl S, Schoenahl F, et al. Is the image quality of I-124-PET impaired by an automatic correction of prompt gammas? *PLoS ONE*. 2013;8:e71729.
- Carlier T, Willowson KP, Fourkal E, Bailey DL, Doss M, Conti M. ⁹⁰Y-PET imaging: exploring limitations and accuracy under conditions of low counts and high random fraction. *Med Phys*. 2015;42:4295.
- Attarwala AA, Molina-Duran F, Büsing K-A, et al. Quantitative and qualitative assessment of yttrium-90 PET/CT imaging. *PLoS One*. 2014;9:e110401.
- Marti-Climent JM, Prieto E, Elosúa C, et al. PET optimization for improved assessment and accurate quantification of ⁹⁰Y-microsphere biodistribution after radioembolization. *Med Phys*. 2014;41:092503.
- Tapp KN, Lea WB, Johnson MS, Tann M, Fletcher JW, Hutchins GD. The impact of image reconstruction bias on PET/CT ⁹⁰Y dosimetry after radioembolization. *J Nucl Med*. 2014;55:1452–1458.
- Sánchez-Crespo A, Andreo P, Larsson SA. Positron flight in human tissues and its influence on PET image spatial resolution. *Eur J Nucl Med Mol Imaging*. 2004;31:44–51.
- Watson CC, Eriksson L, Kolb A. Physics and applications of positron beams in an integrated PET/MR. *Phys Med Biol*. 2013;58:L1–L12.
- Kraus R, Delso G, Ziegler SI. Simulation study of tissue-specific positron range correction for the new Biograph mMR whole-body PET/MR system. *IEEE Trans Nucl Sci*. 2012;59:1900–1909.
- Data RD. Health Physics Society. <http://hps.org/publicinformation/radardecay-data.cfm>. Accessed December 30, 2014.
- Stopping-power and range tables for electrons. National Institute of Standards and Technology website. <http://physics.nist.gov/PhysRefData/Star/Text/ESTAR.html>. Accessed December 30, 2014.
- Selwyn RG, Nickles RJ, Thomadsen BR, DeWerd LA, Micka JA. A new internal pair production branching ratio of ⁹⁰Y: the development of a non-destructive assay for ⁹⁰Y and ⁹⁰Sr. *Appl Radiat Isot*. 2007;65:318–327.